ELSEVIER

Spectrochimica Acta Part B 59 (2004) 1403–1411

SPECTROCHIMICA ACTA PART B

www.elsevier.com/locate/sab

Computer simulations of crater profiles in glow discharge optical emission spectrometry: comparison with experiments and investigation of the underlying mechanisms

Annemie Bogaerts[a,*], Wolfgang Verscharen[b], Edward Steers[c]

[a] *Department of Chemistry, University of Antwerp, Universiteitsplein 1, Wilrijk B-2610, Belgium*
[b] *Birkenweg 11, D-91352 Hallerndorf, Germany*
[c] *London Metropolitan University, 166-220 Holloway Road, London, N7 8DB, UK*

Received 8 March 2004; accepted 10 June 2004
Available online 21 July 2004

Abstract

The crater profiles obtainable with glow discharge sputtering are calculated for a wide range of current–voltage conditions, and comparison is made with experimental data for exactly the same geometry and conditions. The agreement is fairly good, except at high electrical current and low voltage. This good agreement suggests that the model takes into account the correct underlying mechanisms responsible for the crater shape, and that it can be used to predict optimum conditions for flat crater profiles. It is concluded from the model that the characteristic crater shape is determined by the electric potential distribution in front of the cathode, the radial distribution of fluxes and energies of the species bombarding the cathode, as well as the redeposition of sputtered atoms at the cathode surface, which is in correspondence to previous findings.

Keywords: Crater profiles; Glow discharge optical emission spectrometry; Computer simulations; Mechanisms

1. Introduction

Glow discharge optical emission spectrometry (GD-OES) is a powerful technique for depth profiling and thin film analysis of various materials [1–9]. It has been demonstrated that GD-OES is capable of analyzing both layers, which may be considerably thicker than 10 μm (the sputtering rate can be >1 μm/min) and ultrathin films of less than 10 nm thickness [5–7].

For optimum depth resolution, it is crucial that the craters are as flat as possible so that atoms originating from the same depth are sputtered at the same time. In practice, however, glow discharge craters are never perfectly flat; the crater bottom is to some extent either convex or concave, the crater walls are not always very steep, and the crater is sometimes deeper at the sides than in the center [5,7,10–12].

In this paper, we investigate how the crater shape is affected by the discharge conditions (current and voltage), in a comparison between calculations and experiments. Moreover, the model predictions enable us to study the underlying mechanisms responsible for the characteristic crater shapes.

2. Brief description of the modeling network

The modeling network used for these calculations consists of various models (Monte Carlo, fluid and collisional-radiative models) to describe the behavior of the various plasma species. An overview of the plasma species taken into account in this modeling network and the models used to describe their behavior is given in Table 1. Typical calculation results obtained with these models include the electrical characteristics (current–voltage–pressure relations), the electric field and potential distributions in the plasma, the densities, fluxes and energies of the various plasma species, information about their collisions in the

* Corresponding author. Tel.: +32-38202377; fax: +32-38202376.
E-mail address: annemie.bogaerts@ua.ac.be (A. Bogaerts).

0584-8547/$ - see front matter © 2004 Elsevier B.V. All rights reserved.
doi:10.1016/j.sab.2004.06.005

Table 1
Overview of the plasma species considered in the modeling network, and the models used to describe their behavior

Species	Models
Ar gas atoms	No model (assumed uniformly distributed and at room temperature)
Fast electrons	Monte Carlo model
Thermal electrons	Fluid model
Thermal Ar^+ ions	Fluid model
Fast Ar^+ ions in cathode dark space (CDS)	Monte Carlo model
Fast Ar atoms in CDS	Monte Carlo model
Ar atoms in various (64) excited levels, including the metastable levels	Collisional-radiative model
Sputtered flux	Empirical formula
Sputtered atoms (M): thermalization	Monte Carlo model
Sputtered atoms (M) and corresponding ions (M^+)	Fluid model
Fast M^+ ions in CDS	Monte Carlo model

plasma and their formation and loss mechanisms, crater profiles and erosion rates due to sputtering at the cathode, optical emission intensities, etc. More information about this modeling network, the various sub-models and their coupling, as well as the typical calculation results, can be found, for example, in Refs. [13–15]. In this paper, we will focus only on the models, which are directly relevant for the crater profile calculations.

As indicated in Table 1, the sputtered flux J_{sput} (i.e., flux of atoms sputtered from the cathode) is calculated using an empirical formula for the sputtering yield $Y(E)$ as a function of energy of the bombarding particles [16], multiplied by the flux energy distributions $F(E)$ of the plasma species bombarding the cathode, and integrated over all energies:

$$J_{sput} = -\int_E Y(E)F(E)\mathrm{d}E \quad (1)$$

The negative sign indicates that the sputtered flux is in the opposite direction from the fluxes of bombarding species (i.e., away from the cathode vs. towards the cathode).

The plasma species bombarding the cathode, which are responsible for sputtering, are the Ar^+ ions, energetic Ar atoms [created from symmetric charge transfer collisions of Ar^+ ions with Ar atoms in the cathode dark space (CDS)] and the ions (M^+) of the cathode material. Hence, the sputtering yield and flux energy distributions of these three different species must be inserted in Eq. (1). The ions gain energy from the electric field on their way towards the cathode, but they can also lose energy by collisions. This loss mechanism is far more important for the Ar^+ ions than for the M^+ ions due to the efficient loss mechanism by symmetric charge transfer and the higher number density of the Ar atoms. Consequently, the M^+ ions are characterized by much higher energy when bombarding the cathode so that they typically contribute to the sputtering process by a few percent (up to 10%), in spite of their lower flux (see Section 4.2 and Ref. [17]). The energetic Ar atoms are typically characterized by lower energy (because they cannot gain energy from the electric field), but they have a higher flux so that they also play an important role in the sputtering process (see Section 4.2 and Ref. [17]).

When the cathode atoms are sputtered, they typically have energies in the order of a few electron volts, which they rapidly lose by collisions with the Ar gas atoms. Once they are thermalized, their further transport in the plasma is diffusion-dominated. A large fraction of the sputtered atoms, however, will diffuse back towards the cathode and will be redeposited on the cathode surface [12,17]. Hence, the net flux of sputtered atoms is given by: $J_{net,sput} = J_{sput} + J_{redepos}$, where it should be stressed that $J_{redepos}$ is in the opposite direction (i.e., towards the cathode) compared to J_{sput} (i.e., away from the cathode) and hence contains the opposite sign of J_{sput}. This net flux of sputtered atoms gives rise to the erosion rate (and the crater profile after a certain time of sputtering). The erosion rate (ER) is calculated from the net flux of sputtered atoms using Eq. (2) [12]:

$$\mathrm{ER} = J_{net,sput}\frac{M}{N_A\rho} \quad (2)$$

where ER is the erosion rate (in cm/s), $J_{net,sput}$ is the net flux of sputtered atoms (in $cm^{-2}\ s^{-1}$), M and ρ are the atomic weight (g/mol) and density of the sample material [18], respectively, and N_A is the Avogadro number.

Because the modeling network is two dimensional (in cylindrical geometry), the flux energy distributions of the species bombarding the cathode are computed at different

Table 2
Overview of the values of the gas density (in cm^{-3}), assumed as input in the model in order to obtain current–voltage relations in agreement with experiment, for all conditions investigated

Current, I (mA)	Voltage, V (V)								
	380	480	580	680	780	880	980	1080	1180
2		7.3e16	6.5e16	5.7e16	5.1e16	4.7e16	4.3e16	3.9e16	3.5e16
5	9.9e16	9.4e16	8.4e16	7.5e16	7e16	6.4e16	6.1e16	5.2e16	5.1e16
10	1.3e17	1.1e17	9.8e16	9e16	8.6e16	7.9e16	7.6e16	7e16	6.3e16
30	1.6e17	1.5e17	1.4e17	1.3e17	1.2e17	1e17	1e17		
50		1.7e17	1.6e17	1.5e17	1.4e17	1.35e17			

radial positions. We have used 40 radial grid points in our model. Hence, the flux of sputtered atoms and the erosion rate are also calculated as a function of radial position so that the crater profile can be obtained.

3. Experimental

The experimental data were obtained by use of a Spectruma GDA 750 spectrometer. The source was a Grimm-type lamp with an anode diameter of 2.5 mm and an anode–cathode gap of about 0.12 mm. It was operated in the constant voltage mode and the pressure varied to maintain a constant current. The sample was not cooled.

Pure copper plates coated with 10 μm of chemically deposited nickel were used as samples. The samples were polished after coating so the actual layer thickness was a little less than 10 μm. The layer also contained about 12% m/m phosphorus and 0.2% m/m lead. The exact composition may have varied slightly between batches of samples. This material is amorphous. Its relative sputtering rate is about 1.0 compared to iron. A limited number of measurements were made using electrolytically deposited nickel.

The sputtering time required for a layer thickness of about 9 μm (i.e., so that the substrate was almost reached) was calculated using an equation taking into account the nonlinearity of sputtering speed with voltage and current.

Crater profiles were measured by use of a mechanical stylus profilometer "Mahr-Perthometer Concept 6".

4. Results and discussion

4.1. Comparison of calculated and measured crater profiles and erosion rates

The calculations are performed for the Grimm-type source described in Section 3 for exactly the same conditions as in the experiment for five different values of electrical current (i.e., 2, 5, 10, 30 and 50 mA) and for nine different voltage values at every current (i.e., ranging from 380 to 1180 V). The experimental gas temperature was not known. The gas pressure was only measured at some distance from the source, and the measuring device was not calibrated; hence, the measured values are only a rough estimation. Therefore, in the model the Ar gas density (related to gas pressure and temperature, through the ideal gas law: $n = p/kT$) was chosen to obtain the same current–voltage relations as in the experiment. The assumed values of the gas density, for all conditions investigated, are presented in Table 2. We have compared the gas pressure corresponding to these density values with the measured pressure values. As expected, the pressure in the calculations is systematically higher than the measured values (typically a factor of 1.5), but the general trends as a function of voltage and current were very similar.

Although we have previously developed a model that could calculate the gas temperature [19], this model is not included in the present modeling network because it means an additional loop in the calculations, which drastically

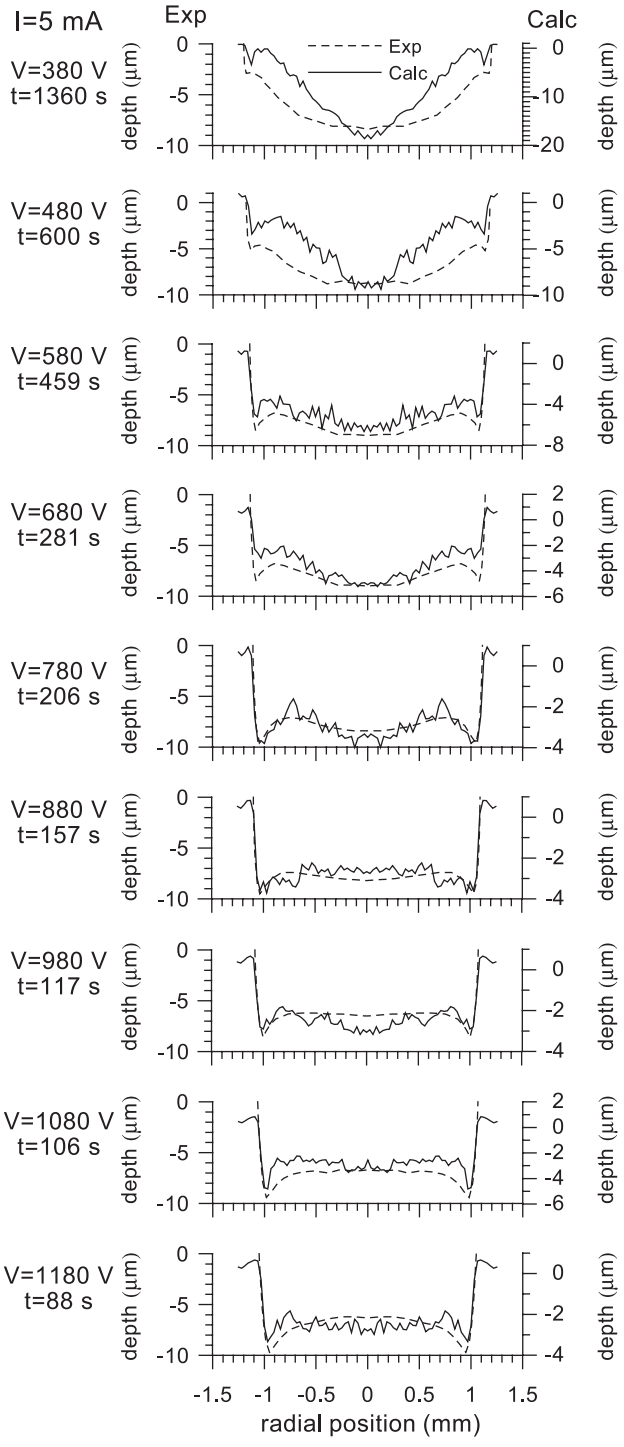

Fig. 1. Measured (left axis, dashed lines) and calculated (right axis, solid lines) crater profiles at a current of 5 mA and different voltages (shown at the left). Also shown at the left are the sputter times used to obtain the crater profiles in both the experiment and the model. Note the differing depth scales of the calculated and measured profiles (left and right axes).

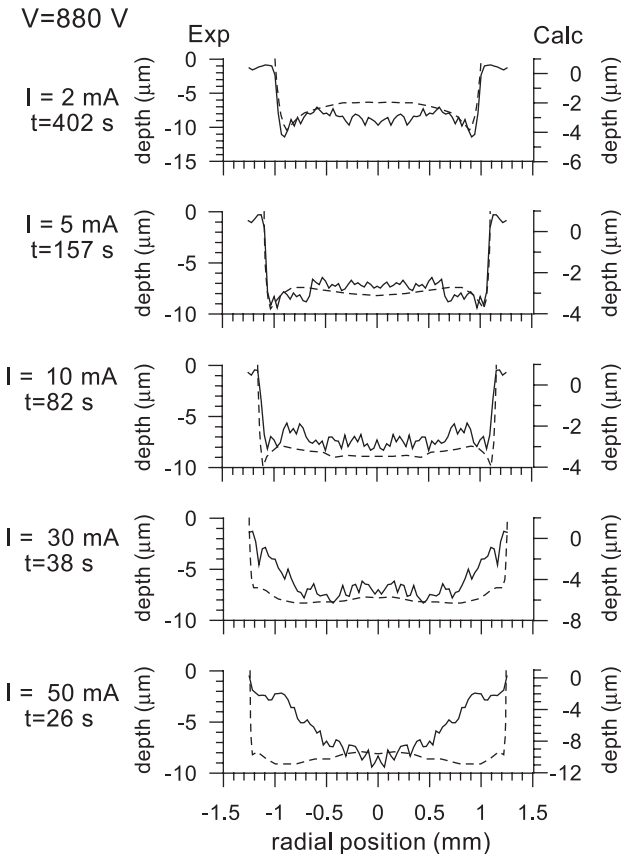

Fig. 2. Measured (left axis, dashed lines) and calculated (right axis, solid lines) crater profiles at a voltage of 880 V and different currents (shown at the left). Also shown at the left are the sputter times used to obtain the crater profiles in both the experiment and the model. Note the differing depth scales of the calculated and the measured profiles (left and right axes).

increases the computation time, and the present calculations were already very time-consuming. Moreover, the gas temperature mainly affects the current–voltage characteristics through the gas density, but since the real gas pressure is not known very accurately from experiment, a precise estimate of the gas density is not attainable anyway. The crater profile itself is probably not affected by the gas temperature profile to a large extent because the gas temperature profile varies mainly in the axial direction [19]. Indeed, as will be shown later, our model with constant gas temperature, and constant gas density, can already back up most of the characteristic trends in the crater profiles.

Finally, although the majority of the measurements were performed for chemically deposited Ni layers containing about 12% m/m phosphorus, we have assumed in the calculations that the cathode was made of pure bulk Ni.

Fig. 1 shows the experimental and calculated crater profiles (left and right axis, dashed and solid lines, respectively) at 5 mA, and for different voltage values. For each case, the sputtering time (used in the experiment and in the model) is also indicated. The agreement between calculated and measured craters is quite reasonable except at the two lowest voltages investigated. At low voltage, both the experiments and the model predict a concave crater shape. At increasing voltage (e.g., 780 V), the crater bottom shows a convex–concave curvature (i.e., deepest at the sides and in the center, and somewhat less deep in between). At still higher voltage, the crater shape becomes convex (i.e., deeper at the sides than in the center). Both the experiments and the model never predict a completely flat crater bottom; however, at 880–980 V, the crater shape can be considered as optimal in both the experimental and the calculated data. Moreover, it is worth mentioning that for most conditions investigated here, the crater shapes are certainly better than in our previous study with the VG9000 source [12].

Fig. 2 illustrates the measured and calculated crater profiles (left and right axis, dashed and solid lines, respectively) at 880 V and five different values of electrical current. The agreement is satisfactory for low current (up to 10 mA), but is worse for 30 and 50 mA. A possible reason is that at this high current, considerable heating of the cathode and of the discharge gas takes place so that the gas in front of the cathode is much hotter (and therefore has a lower density) than in the rest of the discharge. In the model, however, we assume a constant gas density throughout the source so that the assumed gas density in front of the cathode is probably too high in our model. This high gas density (related to high pressure) has certain consequences, such as a very thin CDS and hence a potential strongly varying in space, as well as more scattering by collisions and less efficient radial diffusion (see Section 4.2). The discrepancy with the measured crater profiles suggests that at the high gas density assumed in the model, some of these effects are overestimated. This

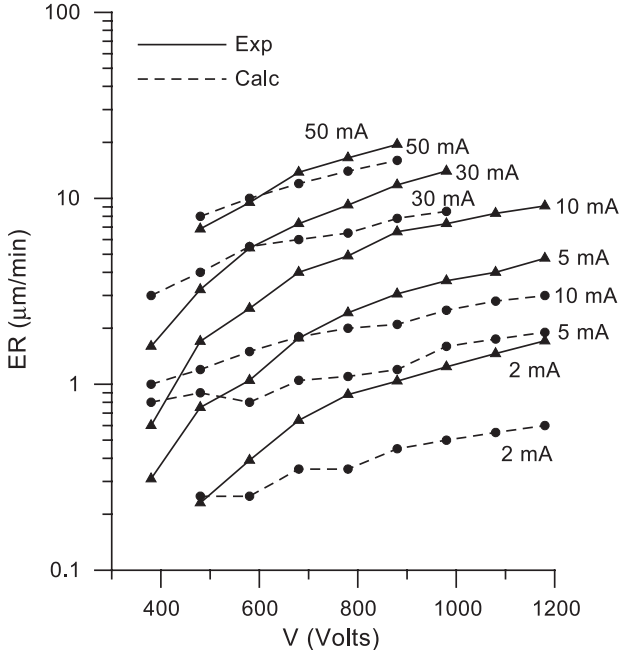

Fig. 3. Measured (solid lines) and calculated (dashed lines) erosion rates due to sputtering, taken as average over the crater region, as a function of voltage at different values of electrical current.

could also explain the discrepancy between experiment and theory at 5 mA and low voltage (380 V) because here the assumed gas density was also fairly high. Moreover, it should be noted that the Spectruma Grimm-type discharge makes use of an additional pumping between sample surface and anode tube so that a pressure gradient, which is not included in the model, can produce differences between model and experiment.

Apart from these points, the general tendency in the crater profiles predicted by the model at increasing electrical current is also found in the experiment with a shift from a convex shape at low current to a flatter shape (or even concave shape in the model) at higher current. Finally, from Fig. 2, it is also clear that at 880 V, a quite flat crater profile is measured at all values of electrical current except at 2 mA.

As mentioned above, the sputter time needed to obtain the craters is also indicated in Figs. 1 and 2 for each voltage–current combination. In the model results, the crater depth is obtained by multiplying the calculated erosion rate with the same sputter time as in the experiment so that comparison can also be made for the absolute values. It appears that the calculated crater depths are in reasonable agreement with the measured ones at low voltage (for the current of 5 mA), but that the calculated erosion rate does not rise so strongly with voltage as in the experiment. Hence, at $V \geq 680$ V, the calculated crater depth is about one half (or less) of the measured depth (see Fig. 1). Similarly, at 880 V, the calculated crater depth is about half of the experimental value for 2, 5 and 10 mA (see Fig. 2). Only at 30 and 50 mA, a better correlation is found. Nevertheless, this discrepancy of a factor of 2–3 between calculated and measured crater depths is considered to be fairly good, if one realizes that the crater profiles are calculated fully self-consistently from the microscopic be-

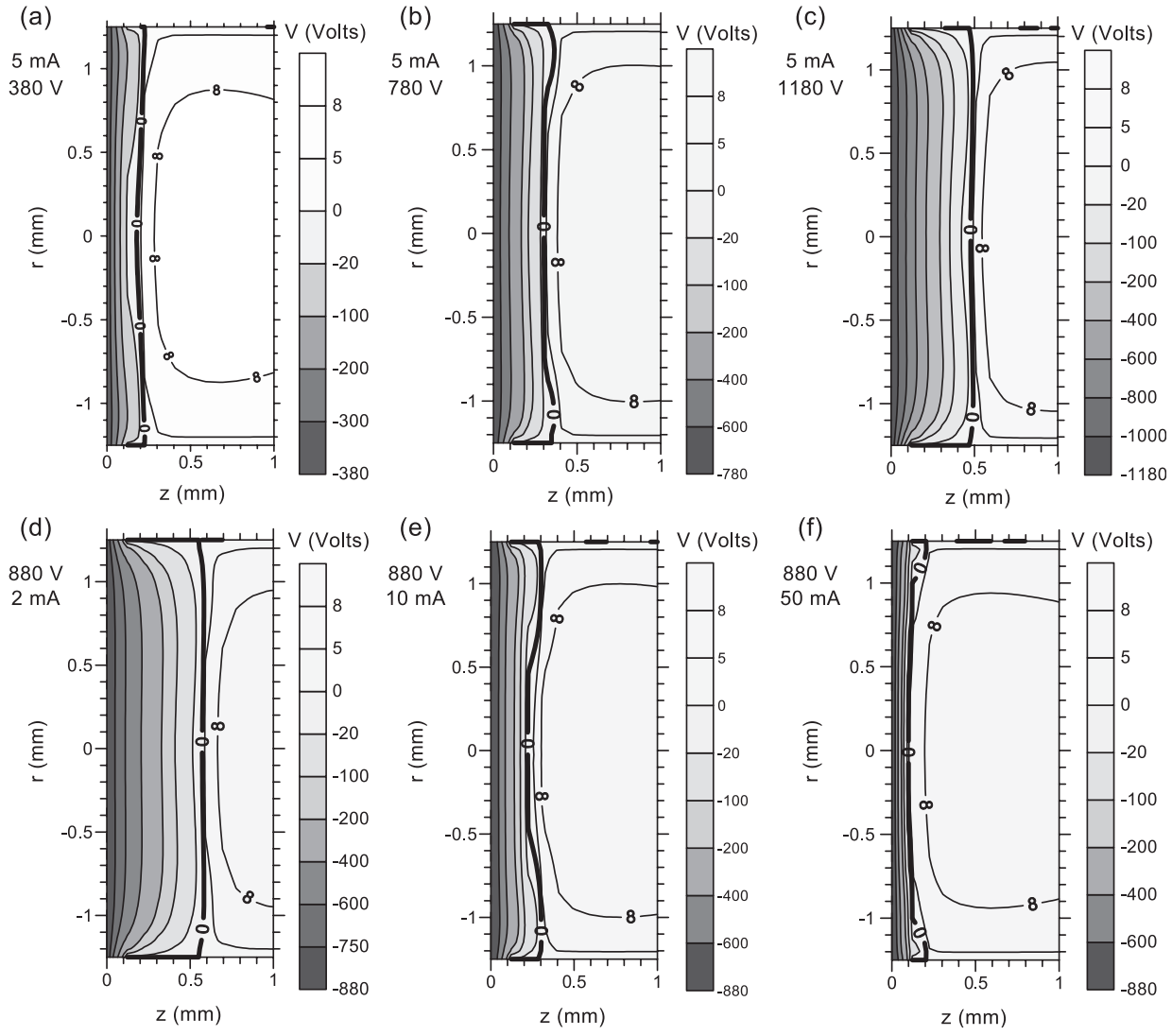

Fig. 4. Calculated potential distributions in the first millimetre in front of the cathode at 5 mA for different voltages [380 V (a), 780 V (b) and 1180 V (c)] and at 880 V for different currents [2 mA (d), 10 mA (e) and 50 mA (f)]. The cathode is found at the left border of the figure ($z=0$). The equipotential line $V=0$, which can be considered as the end of the CDS, is represented with a thicker line.

havior of plasma species using only voltage and current as input data. It should be kept in mind that the model calculations are very complicated and that some input data are subject to considerable uncertainties. For instance, in the model, we have used data of pure bulk Ni to calculate the sputter yield, whereas, in reality, the samples are chemically deposited Ni layers with a significant phosphorus content. Comparison with the limited number of experimental results obtained with electrolytically deposited nickel shows that the crater profile is approximately the same as for chemically deposited layers (there will be a pressure difference so an exact match cannot be expected), but at high voltage and low current, for which the agreement between calculated and experimental profiles is best, the depths are about 25% less for electrolytic nickel and in somewhat better agreement with the calculations.

In Fig. 3, the experimental (solid lines) and calculated (dashed lines) erosion rates (in μm/min), taken as an average over the crater region, are plotted as a function of voltage for different values of electrical current. The experimental erosion rates are deduced from the measured crater depth after the indicated time of sputtering. It is indeed clear from Fig. 3 that the calculated erosion rates are a factor of 2–3 lower than the measured values at low currents (2, 5 and 10 mA) because the rise of erosion rate with voltage, as predicted in the model, is not so pronounced as in the experiment. However, at 30 and 50 mA, the correlation is better and the overall agreement is satisfactory (i.e., general tendency, as well as order of magnitudes).

4.2. Underlying mechanisms responsible for the crater shapes

Because the calculated crater profiles, as well as the behavior as a function of voltage and current, are in reasonable agreement with the experimental observations, the model can be used to try to explain the crater shape from the microscopic point of view, i.e., based on the behavior of the various plasma species. The origin of the specific crater shape was also investigated in previous work [10–12], but the model enables us to quantify the effects and their relative importance for different conditions.

4.2.1. Potential distribution

The crater arises from sputtering, resulting from the bombardment of Ar^+ ions, fast Ar atoms (which are formed directly from collisions of Ar^+ ions) and (sputtered material) Ni^+ ions at the cathode. Since the ions are directed towards the cathode by the strong electric field in the CDS, we first need to investigate the potential distribution in front of the cathode. Fig. 4(a–f) shows the calculated equipotential lines in the first millimetre in front of the cathode for six different conditions: at constant current (5 mA) for three different voltages [380 V (a), 780 V (b) and 1180 V (c)] and at constant voltage (880 V) for three different currents [2 mA (d), 10 mA (e) and 50 mA (f)]. The cathode is found at the left border of the figure ($z=0$), and the thicker equipotential line ($V=0$) shows the end of the CDS as defined in this work.

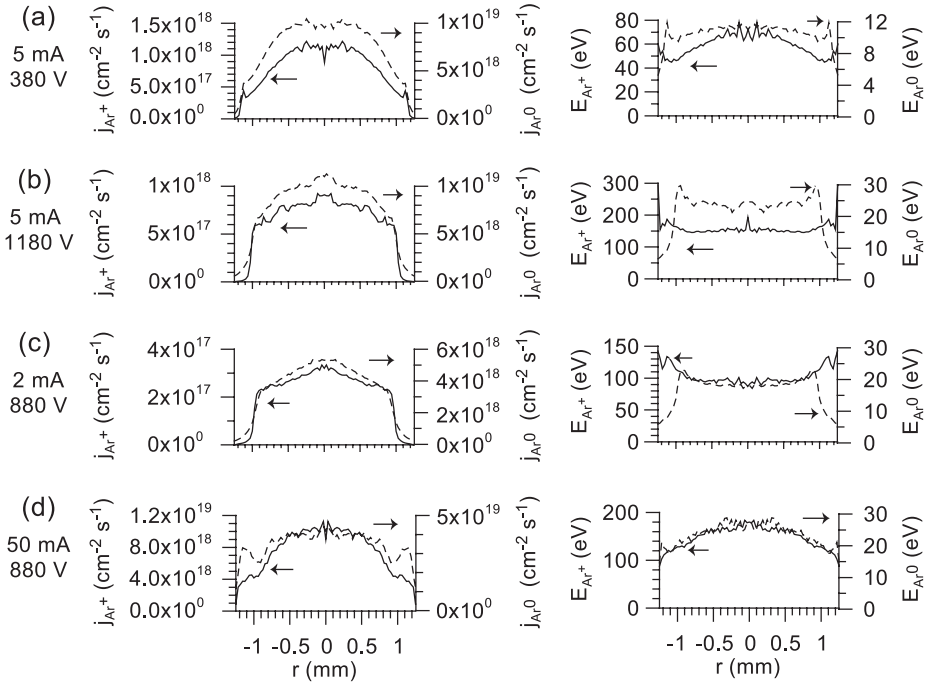

Fig. 5. Calculated fluxes (left column) and average energies (right column) of Ar^+ ions (left axes, solid lines) and fast Ar atoms (right axes, dashed lines) bombarding the cathode as a function of radial position at 5 mA for two different voltages [380 V (a) and 1180 V (b)] and at 880 V for two different currents [2 mA (c) and 50 mA (d)].

In general, the equipotential lines are quite parallel to each other and to the cathode surface so that the bottom of the crater is also expected to be more or less flat for most conditions investigated. This was indeed found in the calculated and experimental results (Figs. 1 and 2). It illustrates that the Grimm-type source is well suited for depth profiling in contrast to, for instance, the VG9000 flat cell [12]. Indeed, for the latter cell geometry, our model predicted a strong curvature in the equipotential lines in front of the cathode (see Fig. 4 of Ref. [12]) due to the anode frontplate at a distance of 0.5 mm from the cathode; consequently, the resulting crater was predicted to be much deeper at the sides than in the center, which is in agreement with experimental observations [12]. In the Grimm-type source, the anode cell body is at a distance of 0.2 mm from the cathode (sample), but because of the higher pressure used in the Grimm-type source, the CDS is much thinner (order of 0.1–0.6 mm compared to several millimetres at typical pressures of the VG9000 cell [12]), and the anode cell body does not affect the equipotential lines to a large extent.

It is also clear from Fig. 4 that the CDS becomes thicker at increasing voltage for constant current and at decreasing current for constant voltage. Both a rise in voltage at constant current and a drop in current at constant voltage are correlated to a drop in pressure. In other words, the CDS becomes thicker for lower pressure as expected [13,14]. Looking carefully, Fig. 4 shows that the equipotential lines at 380 V and 5 mA (a) and at 880 V and 50 mA (f), i.e., at low voltage for a certain current and at high current for a certain voltage, are a bit more curved, coming closer to each other near the cell axis. This results in a somewhat stronger electric field so that in these cases, slightly higher energies can be expected for ions bombarding the middle of the cathode.

4.2.2. Fluxes and energies of the bombarding plasma species

To study the bombardment of the plasma species in more detail, the fluxes and average energies of the Ar^+ ions and fast Ar atoms bombarding the cathode are plotted as a function of radial position in Fig. 5(a–d) for four different conditions: at constant current (5 mA) for a low and a high voltage [380 V (a) and 1180 V (b), respectively] and at constant voltage (880 V) for a low current [2 mA (c)] and a high current [50 mA (d)]. Note that the fluxes yield the number of ions/atoms bombarding the cathode (per time and surface area) and the energies determine the efficiency of sputtering (since a higher bombarding energy results in higher sputter yields). Hence, both flux and energy are important to determine the amount of sputtering.

However, before drawing conclusions on this figure, we first need to know the relative role of these species in the sputtering process. This is illustrated in Fig. 6 as a function of voltage at 5 mA (a) and as a function of current at 880 V (b) not only for the Ar^+ ions and fast Ar atoms but also for the metal (Ni^+ ions). The Ar^+ ions contribute 30–70%, and their role increases with decreasing voltage and with rising

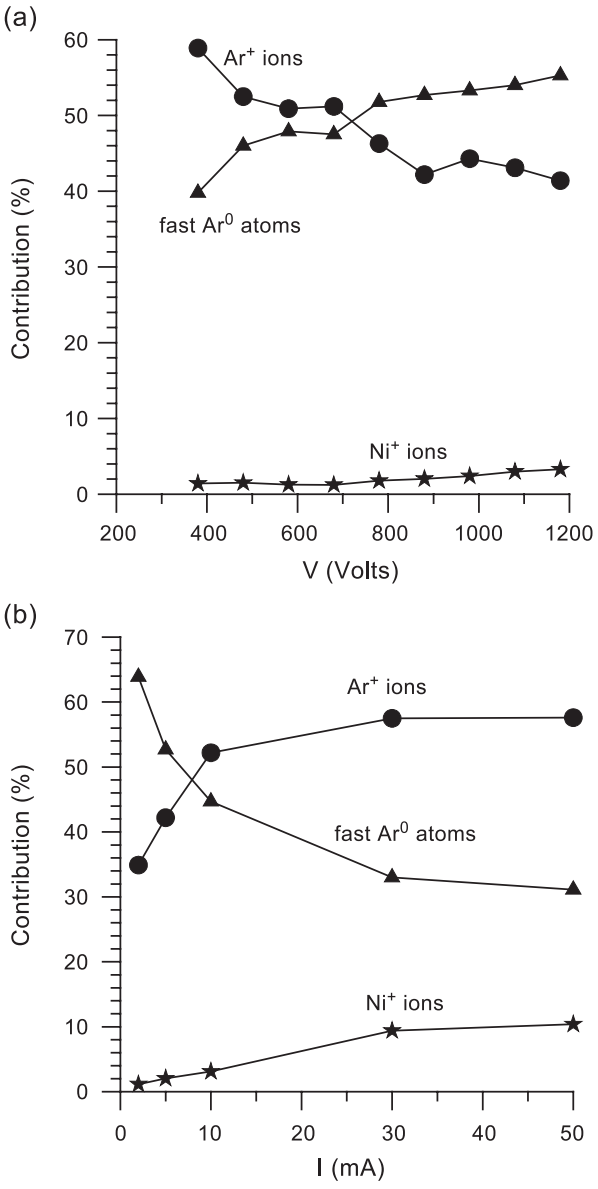

Fig. 6. Calculated contributions of Ar^+ ions, fast Ar atoms and Ni^+ ions to the sputtering process as a function of voltage at 5 mA (a) and as a function of current at 880 V (b).

current. The contribution of fast Ar atoms is in the same range, but increases with rising voltage and with decreasing current. The reason for this significant contribution of fast Ar atoms is their large flux bombarding the cathode (cf. Fig. 5). The role of Ni^+ ions in the sputtering process increases with voltage and current, but was never calculated more than about 10%. For this reason, the fluxes and energies of Ni^+ ions were not included in Fig. 5. Moreover, in studying Fig. 5, we should focus especially on the Ar^+ ions at low voltage or high current and on the fast Ar atoms at high voltage or low current.

Looking back at Fig. 5 and concentrating first on the effect of voltage at constant current [Fig. 5(a,b)], it is clear that at low voltage [380 V (a)], the flux profiles of Ar^+ ions

and fast Ar atoms are more parabolic in shape, whereas they are flatter at high voltage [1180 V (b)]. The reason is that a lower voltage, at a certain current, correlates with a higher gas pressure, for which diffusion is less efficient. Hence, at high pressure, the Ar^+ ion density has a more pronounced maximum near the cell axis, whereas it is more spread out radially by diffusion at lower pressure. Besides the flux profiles, the energies of Ar^+ ions (and fast Ar atoms) are at maximum at the middle of the cathode at low voltage (a), which is a result of the somewhat stronger electric field (cf. Fig. 4), whereas at high voltage, the energy of the Ar^+ ions is nearly constant as a function of radial position and the energy of the fast Ar atoms is minimum at the center and reaches a maximum at about 1 mm from the center. Hence, the combination of flux and energy will give rise to a more or less constant sputter flux over the cathode surface at high voltage, whereas at low voltage, the highest sputter flux is expected in the middle of the cathode.

A similar conclusion can be drawn from the effect of electrical current at constant voltage [880 V; Fig. 5(c,d)]. At low current [2 mA (c)], the fluxes of Ar^+ ions and fast Ar atoms reach a small maximum at the center of the cathode, but the energies are lowest here and are at maximum at about 1 mm from the center so that the combination of flux and energy yields again a quite constant sputter flux over the cathode surface. At high current [50 mA (d)], on the other hand, the Ar^+ ion flux shows a stronger variation over the radial direction (i.e., less flat), which is again the result of less efficient radial diffusion and hence the more peaked Ar^+ ion density at high current (high pressure). Moreover, the Ar^+ ion and fast Ar atom energy are also higher near the center of the cathode because of the somewhat stronger electric field at high current (cf. Fig. 4). Hence, at high current, the sputter flux is expected to be higher at the center than at the sides of the cathode.

4.2.3. Effect of redeposition of sputtered atoms at the cathode surface

These trends (i.e., higher sputtering at the center for low voltage at a certain current and for high current at a certain voltage compared to more constant sputtering over the cathode surface at high voltage and lower current) show already a good correlation with the calculated and measured crater profiles (cf. Figs. 1 and 2). However, it should be realized that the final crater profile is not only determined by the sputter flux, but also by the flux of back-diffusing atoms that are redeposited on the cathode surface (see above). Hence, Fig. 7(a–d) shows, for the four conditions investigated above, the total sputter flux as a function of radial position at the cathode as well as the back-diffusion flux (resulting in redeposition) and the resulting net flux of sputtering, which gives the final crater profile.

It is clear from this figure that at low voltage for a certain current [5 mA, 380 V (a)] and at high current for a certain voltage [880 V, 50 mA (d)], the total sputter flux has a maximum in the center and the back-diffusion flux and net sputter flux have a similar profile. Hence, the latter yields a concave crater shape as is clear from Figs. 1 and 2. At higher voltage for the same current [5 mA, 1180 V (b)] and at low current for the same voltage [880 V, 2 mA (c)], the total

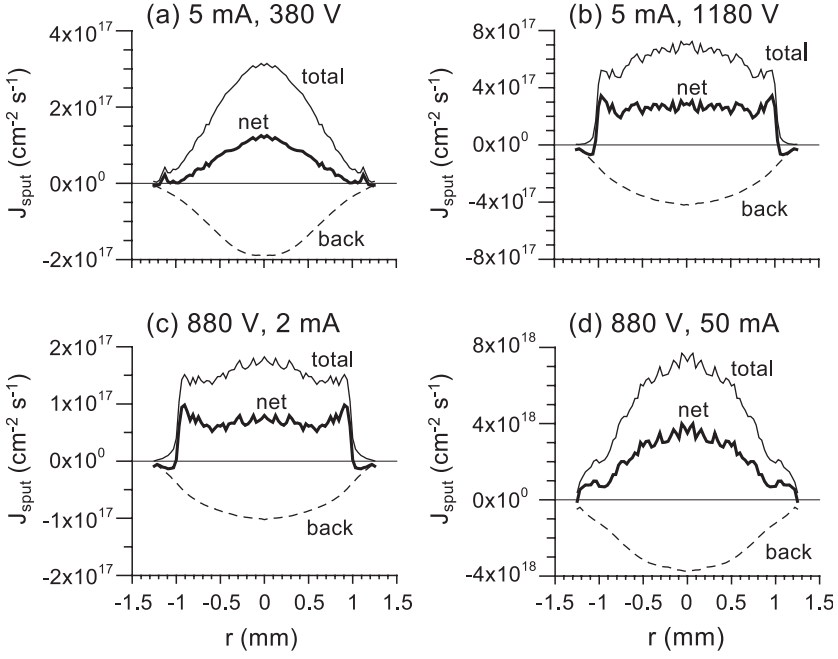

Fig. 7. Calculated total sputter fluxes (thin solid lines), fluxes of back-diffusing atoms redepositing at the cathode surface (thin dashed lines) and net sputter fluxes from the cathode (thick solid lines) as a function of radial position at 5 mA for two different voltages [380 V (a) and 1180 V (b)] and at 880 V for two different currents [2 mA (c) and 50 mA (d)].

sputter flux is flatter; however, because the back-diffusion flux is always at maximum near the center (since the sputtered Ni atom density has a maximum at the cell axis), the net flux of sputtering can be higher at the sides, giving rise to a convex crater shape. The latter is indeed found in both the calculated and the measured crater profiles (cf. Figs. 1 and 2).

5. Conclusion

We have calculated crater profiles due to glow discharge sputtering in a Grimm-type source, for a wide range of voltage–current conditions. Comparison has been made with experimental data for exactly the same cell geometry and discharge conditions, and the agreement is fairly good, except at very low voltages and high electrical currents. The reason for this small discrepancy is probably that the gas density (related to gas pressure) assumed in the model was too high and that the effects occurring at high gas pressure (such as a very thin CDS, more scattering by collisions and less efficient radial diffusion) are a bit overestimated in the model. However, the general agreement between calculations and experiments is quite satisfactory. Hence, this suggests that the model takes into account the correct underlying mechanisms responsible to the characteristic crater shapes.

It was indeed found that the crater shape can be explained based on the calculated potential distribution in front of the cathode, the fluxes and energies of plasma species bombarding the cathode and the flux of back-diffusing (redepositing) atoms at the cathode surface.

At high current for a certain voltage (e.g., 50 mA, 880 V) or at low voltage for a certain current (e.g., 5 mA, 380 V), both the fluxes and energies of Ar^+ ions and fast Ar atoms reach a maximum at the center so that the total sputter flux, as well as the net sputter flux, are also at maximum at the center. This results in a concave crater shape as is indeed found back in the calculations and in the experiments (to a less extent).

On the other hand, at low current for a certain voltage (e.g., 2 mA, 880 V) or at high voltage for a certain current (e.g., 5 mA, 1180 V), the fluxes of Ar^+ ions and fast Ar atoms are quite constant over the cathode surface, or they show only a small maximum near the center, but this is compensated by a somewhat higher energy near the sides. Hence, the combination of fluxes and energies gives rise to a nearly constant total sputter flux over the cathode surface. Because the flux of back-diffusing atoms is at maximum at the cathode center, the net sputter flux is somewhat higher near the sides, giving rise to a slightly convex crater shape as is also found back in the calculations and experiments.

Acknowledgments

A. Bogaerts acknowledges financial support from the Flemish Fund for Scientific Research (FWO) and the Belgian Science Policy through IUAP-V.

References

[1] K. Shimizu, H. Habazaki, P. Skeldon, G.E. Thompson, G.C. Wood, GDOES depth profiling analysis of amorphous Ni–P-plated aluminium hard disks, Surf. Interface Anal. 29 (2000) 151–154.
[2] J. Pisonero, C. Perez, R. Pereiro, N. Bordel, A. Sanz-Medel, In-depth profile analysis by radiofrequency glow discharge optical emission spectrometry using pressure as variable parameter, J. Anal. At. Spectrom. 16 (2001) 370–375.
[3] R.K. Marcus, A.B. Anfone, W. Luesaiwong, T.A. Hill, D. Perahia, K. Shimizu, Radio-frequency glow discharge optical emission spectroscopy: a new weapon in the depth profiling arsenal, Anal. Bioanal. Chem. 373 (2002) 656–663.
[4] B. Fernandez, N. Bordel, R. Pereiro, A. Sanz-Medel, Investigations of the effect of hydrogen, nitrogen or oxygen on the in-depth profile analysis by radio-frequency argon glow discharge optical emission spectrometry, J. Anal. At. Spectrom. 18 (2003) 151–156.
[5] J. Angeli, A. Bengtson, A. Bogaerts, V. Hoffmann, V.-D. Hodoroaba, E. Steers, Glow discharge optical emission spectrometry: moving towards reliable thin film analysis—a short review, J. Anal. At. Spectrom. 18 (2003) 670–697.
[6] K. Shimizu, H. Habazaki, P. Skeldon, G.E. Thompson, Impact of RF-GD-OES in practical surface analysis, Spectrochim. Acta Part B 58 (2003) 1573–1583.
[7] K. Shimizu, H. Habazaki, P. Skeldon, G.E. Thompson, Radiofrequency GDOES: a powerful technique for depth profiling analysis of thin films, Surf. Interface Anal. 35 (2003) 564–574.
[8] V. Hoffmann, R. Dorka, L. Wilken, V.-D. Hodoroaba, K. Wetzig, Present possibilities of thin-layer analysis by GDOES, Surf. Interface Anal. 35 (2003) 575–582.
[9] P. Le Coustumer, M. Motelica-Heino, P. Chapon, H.F. Saint-Cyr, R. Payling, Surface characterization and depth profile analysis of glasses by RF GDOES, Surf. Interface Anal. 35 (2003) 623–629.
[10] Z. Weiss, Quantitative evaluation of depth profiles analysed by glow discharge optical emission spectroscopy: analysis of diffusion processes, Spectrochim. Acta Part B 47 (1992) 859–876.
[11] N. Jakubowski, D. Stüwer, Application of glow discharge mass spectrometry with low mass resolution for in-depth analysis of technical surface layers, J. Anal. At. Spectrom. 7 (1992) 951–958.
[12] A. Bogaerts, R. Gijbels, Calculation of crater profiles on a flat cathode in a direct current glow discharge, Spectrochim. Acta Part B 52 (1997) 765–777.
[13] A. Bogaerts, R. Gijbels, Modeling of argon direct current glow discharges and comparison with experiment: how good is the agreement? J. Anal. At. Spectrom. 13 (1998) 945–953.
[14] A. Bogaerts, Comprehensive modeling network for DC glow discharges in argon, Plasma Sources Sci. Technol. 8 (1999) 210–229.
[15] A. Bogaerts, R. Gijbels, Numerical modeling of analytical glow discharges, in: R.K. Marcus, J.A.C. Broekaert (Eds.), Glow Discharge Plasmas in Analytical Spectroscopy, Wiley, Chichester, 2003, pp. 155–205, Chap. 6.
[16] N. Matsunami, Y. Yamamura, Y. Itikawa, N. Itoh, Y. Kaxumata, S. Miyagawa, K. Morita, R. Shimizu, H. Tawara, Energy dependence of the ion-induced sputtering yields of monoatomic solids, At. Data Nucl. Data Tables 31 (1984) 1–80.
[17] A. Bogaerts, R. Gijbels, Role of sputtered Cu atoms and ions in a direct current glow discharge: combined fluid and Monte Carlo model, J. Appl. Phys. 79 (1996) 1279–1286.
[18] D.R. Lide, CRC Handbook of Chemistry and Physics, 83rd edition, CRC Press, Boca Raton, 2002–2003.
[19] A. Bogaerts, R. Gijbels, V.V. Serikov, Calculation of gas heating in direct current argon glow discharges, J. Appl. Phys. 87 (2000) 8334–8344.